2D multiphysics model for proton conductor ceramic technology investigating the effects of temperature, composition of reactants and electrolyte material

Journal of Power Sources 663 (2026) 238898

Contents lists available at ScienceDirect

Journal of Power Sources

journal homepage: www.elsevier.com/locate/jpowsour

2D multiphysics model for proton conductor ceramic technology investigating the effects of temperature, composition of reactants and electrolyte material

Andrea Moranti [a,*], Domenico Ferrero [a], Francesco Da Prato [a], Simone Anelli [b], Federico Smeacetto [b], Massimo Santarelli [a]

[a] Department of Energy (DENERG), Politecnico di Torino, 10129, Turin, Italy
[b] Department of Applied Science and Technology (DISAT), Politecnico di Torino, 10129, Turin, Italy

HIGHLIGHTS

- 2D thermo-fluid-dynamic-electrochemical model of protonic ceramic electrolysis.
- Sensitivity analysis of operating conditions on the electrolysis performance.
- BCZY improves proton transport and faradaic efficiency compared to BZY20.
- Higher water content at electrodes enhances faradaic efficiency.
- Increased temperature raises proton diffusivity but lowers proton concentration.

ARTICLE INFO

Keywords:
Protonic Ceramic Cells (PCC)
Hydrogen production
Energy storage
Current leakage
Planar cell
Thermodynamic parameters

ABSTRACT

The main goal of this work is the development of a model for a protonic ceramic electrolysis cell (PCEC), a technology emerging as a promising alternative to traditional solid oxide cells (SOCs). A two-dimensional numerical model has been developed for the simulation of a planar cell (5 × 5 cm^2). The model is set up as the combination of a thermal-fluid-dynamic model and an electro-chemical one, also comprehending the transport of three defects (protons, electron holes and oxygen vacancies) through the membrane, typical for barium-based zirconate. Firstly, a state-of-the-art $BaZr_{0.8}Y_{0.2}O_{3-\delta}$ (BZY) electrolyte material and cell structure (electrode supported Ni-BZY/BZY/SFM-BZY) with available experimental performance data have been selected from literature. Furthermore, the parameters required to model a novel material $BaCe_{0.65}Zr_{0.2}Y_{0.15}O_{3-\delta}$ (BCZY), still not available in literature, have been introduced. The purpose of this study is to quantify the effect of different operating conditions and modeling assumptions on the hydrogen production performance for the state of the art BZY electrolyte, also establishing the effect of the electronic leakage on the transport number and faradaic efficiency. Finally, this material is compared to the newly introduced BCZY to assess their respective advantages and disadvantages.

1. Introduction

The increasing world's energy consumption [1] and the environmental issues originating from fossil fuels being employed as sources are being tackled by exploiting renewable energy sources (RES). However, RES are characterized by issues such as intermittency and lack of programmability and therefore require solutions able to balance electrical power consumption, storage, and production [2]. At the same time, sustainable chemistry asks for molecules that guarantee a continuous and recyclable balance between reactants and products, considering Carbon (no new carbon added in the atmosphere).

In this context, looking at the available technologies, protonic ceramic cells (PCCs) are attracting growing interest. The interest shown in protonic ceramic cells, especially in comparison to solid oxide cells (SOCs) based on oxygen-ion conducting electrolytes, including lower activation energy due to hydrogen ion (H^+) conduction, higher

* Corresponding author.
E-mail address: andrea.moranti@polito.it (A. Moranti).

https://doi.org/10.1016/j.jpowsour.2025.238898
Received 12 December 2024; Received in revised form 7 October 2025; Accepted 17 November 2025
Available online 27 November 2025

theoretical efficiency, and reduced Balance of Plant requirements. They also exhibit better resistance to H_2S poisoning, enabling the use of alternative fuels with less extensive desulphurization. Lower operating temperatures reduce degradation and enhance long-term efficiency, making PCCs suitable for electrolysis and fuel cell applications. However, challenges remain, including issues with reaction processes, conductivity, durability, and scalability.

PCCs have potential in traditional electrolysis and fuel cells, as well as in emerging applications like advanced sensors [3], hydrogen separation, and the production of high-purity hydrogen [4] and chemicals such as ammonia and methane [5] as sources are being tackled by exploiting renewable energy sources (RES). However, RES are characterized by issues such as intermittency and lack of programmability and therefore require solutions able to balance electrical power consumption, storage, and production [2]. At the same time, sustainable.

PCCs were initially investigated in the 1980s with electrolytes made of barium cerate perovskite ($BaCe_{1-x}Y_xO_{3-\delta}$) [6], material that exhibits proton conductivity already at moderate temperatures, between 400 and 600 °C, enabling cost-effective operation [7]. Its high reactivity in CO_2 and H_2O environments, though, makes it impractical for some applications. The alternative barium zirconate perovskite ($BaZr_{1-x}Y_xO_{3-\delta}$) was therefore explored due to its higher chemical stability [6], associated with the closer ionic radius and electroneutrality between zirconium and yttrium [8,9], the crystal structure of BZO, the shorter and stronger Zr-O bonds, and the bond length distances between Zr-O and Ba-O [10].

Considering the low technological readiness level of this technology, current research on proton-conducting electrolytes is focusing on materials that combine yttrium-doped barium cerate and zirconate perovskite. The goal is to achieve a trade-off between BZY, which offers greater stability, and BCY, which provides higher conductivity but is less durable in H_2O and CO_2 environments [6]. This is experimentally obtained throughout variable stoichiometry of Zr and Ce in the perovskite to obtain different zirconium and cerium doped barium perovskite ($BaCe_yZr_{1-x-y}Y_xO_{3-\delta}$). Higher contents of cerium, and consequently lower zirconium, will therefore increase the ionic conductivity, while higher zirconium will improve the chemical stability. Additionally, studies are being conducted on sintering aids to address manufacturing process issues [11].

One of the main disadvantages, when proton conducting perovskite materials are used for the electrolyte, is the current leakage. When compared to solid oxide cells, which operate by transmitting oxygen ions (O^{2-}) through the electrolyte, the protonic ceramic cells are characterized by a mixed ionic electronic conductor (MIEC) electrolyte membrane that transmits three mobile charge-carrying defects: protons, oxygen vacancies, and electron holes, usually defined as O-site polarons when attributed to an oxygen site [12–14]. O-site polarons may also be trapped in the yttrium dopant, as considered in this work [15]. The multiple mobile defects impact negatively the performance of the cell by producing a loss of potential, in both open and closed circuits, as well as increasing the resistive losses through the membrane [12].

When considering the electrolysis application, molecular hydrogen (H_2) is produced at the cathode through the reduction of protons passing through the membrane, according to the reaction:

$$2H^+ + 2e^- \rightarrow H_2$$

The opposite electrode is the steam electrode (anode), where the water splitting produces molecular oxygen (O_2), protons and electrons through the following oxidation reaction:

$$H_2O \rightarrow 1/2O_2 + 2H^+ + 2e^-$$

Both water oxidation reaction (WOR) and hydrogen reduction reaction (HRR) occur in the mixed ion and electronic conducting (MIEC) electrodes and are confined to the triple phase boundaries (TPBs) where ion, electron and gas phases meet. It would be therefore also desirable to introduce proton conduction in the MIEC material to produce a triple conducting oxide (TCO). At the current state, it is still hard to produce sufficient defects for proton conduction with available hydrated oxygen vacancies [16–18].

Some models have already been implemented for proton conductor ceramic cells in fuel cells, both traditional [19–21] or fed by alternative fuels [22–25] and for electrolyzers [26,27]. However, these models neglect the multiple defects transport and the corresponding impact on the performance.

On this aspect, several studies have been performed, even though for a limited variety of materials, to present models with a unidimensional approach [12–15,28].

Finally, only a limited number of studies implement models in fuel cells and especially electrolysis mode [29–31], for entire cells and considering the presence of multiple defects during the operation. Still, most recent work does not consider the polaron trapping which instead has been accounted for in this work. Furthermore, almost in all available literature, the membranes are modeled using the thermodynamic parameters for the BZY electrolyte material. This aspect has also been tackled by adding thermodynamic parameters, not available in literature, for the material ($BaCe_{0.65}Zr_{0.2}Y_{0.15}O_{3-\delta}$) comparing them to the state-of-the-art BZY. Finally, also different assumptions in terms of thermodynamic properties and compressibility for the fluids have been considered.

Hence, in this study, a multi-physics fluidic, thermal, and electric two-dimensional model for a proton conductive electrolysis cell is implemented considering the motion of three defects, including the trapping of the polarons when interacting with the yttrium dopant. The materials selected for the electrolyte, cathode and anode, are respectively yttrium-doped barium zirconate ($BaZr_{0.8}Y_{0.2}O_{3-\delta}$), abbreviated as BZY in this work, nickel and electrolyte material composite (Ni-BZY), and composite between molybdenum doped strontium ferrite (SFM) and BZY (SFM-BZY).

This study first extends the modeling approach already available in literature to a novel electrolyte material, BCZY, whose thermodynamic parameters are not available in the literature. One of the objectives of introducing BCZY into the model in comparison to the well-established BZY, is to provide a quantitative assessment of how different electrolyte compositions influence operational performance. This includes evaluating hydrogen production rates, electronic leakage, and key transport properties. Furthermore, another contribution is the additional and detailed quantification of how different operating conditions, such as temperature and gas compositions, affect performance metrics, also considered as critical for understanding the applicability of these materials providing inputs for future development of the technology."

2. Materials and methods

2.1. Cell geometry

The model has been implemented for a single cell, having the structure shown in Fig. 1.

The cell shown, with size 5×5 cm^2, is composed, from the outermost to the innermost, of dual channels for fluidic and electronic purposes with segregated flow paths, porous electrodes divided into gas diffusion electrodes and gas diffusion layers and membrane with defects transport. Each one of these elements will be further described in the following sections.

The cell is assumed to operate in a steady state condition. Heat transfer is imposed throughout all the layers. The boundary conditions defined at the inlet for the fluids are 1) flow rate (both channels), 2) inlet flow composition, and 3) inlet temperature. Boundary conditions were chosen according to the reference used from literature [32]. The cell operates at ambient pressure. Regarding the electrical model, the electric potential is imposed at the electrode/interconnect interface boundary with the ground on the cathodic side. The channels are

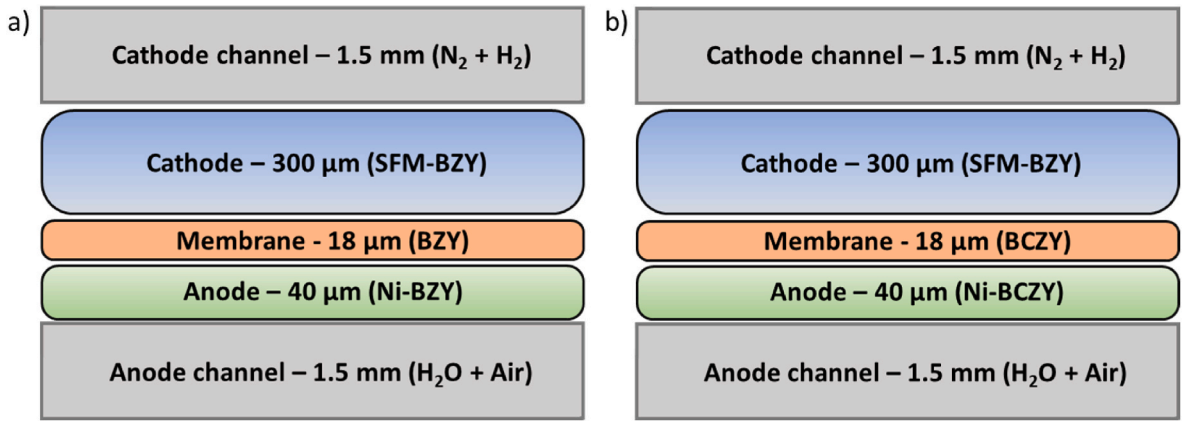

Fig. 1. Cells structure with a) BZY and b) BCZY electrolytes showing the thickness and composition for each layer.

assumed equipotential to the set values.

Finally, a detailed description of the multi-physics is described in the following sections.

2.2. Membrane model and thermodynamic parameters estimation

2.2.1. Nernst-Planck-Poisson problem

As already mentioned, in the membrane the three mobile charge-carrying defects, written using the Kröger-Vink notation, are assumed to be respectively the protons $(OH_o^{\cdot})$, oxygen vacancies $(V_o^{\cdot\cdot})$ and electron holes $(h^{\cdot})$ which, when assumed to be located in an oxygen site, constitute a positive polaron $(O_o^{\cdot})$ [28]. These last defects are also assumed to interact with a portion of the dopant yttrium in the B-site (Y'_{X_B}), producing a trapped polaron $(Y'_{X_B} - O_o^{\cdot})$. Furthermore, in the Kröger-Vink notation, also the neutral oxygen site is used (O_o^x). The model setup and the parameters used for the BZY material have been defined according to the research available in literature from Zhu et al. [15].

The incorporation reactions occurring between gas and electrolyte interface can be described and modeled according to the equilibrium constant (K_P), defined in terms of gas partial pressure (p). Both the reactions and corresponding constants can be summarized as:

- Interface with hydrogen:

$$\frac{1}{2}H_2 + O_o^{\cdot} \leftrightarrow OH_o \quad [1]$$

$$K_{P,H2} = \frac{[OH_o^{\cdot}]_L}{[O_o^{\cdot}]_L \cdot p_{H2}^{1/2}} \quad [2]$$

- Interface with oxygen:

$$\frac{1}{2}O_2 + O_o^x + V_o^{\cdot\cdot} \leftrightarrow 2O_o^{\cdot} \quad [3]$$

$$K_{P,O2} = \frac{[O_o^{\cdot}]_L^2}{[O_0^x]_L p_{O2}^{1/2}} \quad [4]$$

- Interface with water:

$$H_2O + V_o^{\cdot\cdot} + O_o^x \leftrightarrow 2OH_o \quad [5]$$

$$K_{P,H2O} = \frac{[OH_o^{\cdot}]_L^2}{[O_o^x]_L \cdot [V_o^{\cdot\cdot}]_L \cdot p_{H2O}} \quad [6]$$

- Polaron trapping:

$$Y'_{X_B} + O_o^{\cdot} \leftrightarrow \left(Y'_{X_B} - O_o^{\cdot}\right) \quad [7]$$

$$K_{P,Trap} = \frac{\left[\left(Y'_{X_B} - O_o^{\cdot}\right)\right]_L}{\left[Y'_{X_B}\right]_L \cdot [O_o^{\cdot}]_L} \quad [8]$$

The subscript (L) is used to represent the formula unit concentration, estimated through the equation $[X_k]_L = [X_k] \cdot V_m$ with V_m representing the lattice molar volume. The equilibrium constants can be evaluated through the equation $K_P = \exp\left(\frac{\Delta S^\circ}{R}\right) exp\left(-\frac{\Delta H^\circ}{RT}\right)$. All of the constants are coupled by the gas-phase reaction $H_2 + \frac{1}{2}O_2 \leftrightarrow H_2O$ through the relation $K_{P,H2}^2 K_{P,O2} = K_{P,H2O} K_{P,gas-phase}$. The values of V_m for the BZY electrolyte employed is $4.57 \cdot 10^{-5} \frac{m^3}{mol}$.

Finally, the value for the equilibrium constant of the hydrogen interaction with the perovskite can be estimated via Equation (9), while the thermodynamic parameters are evaluated according to Equations (10) and (11).

$$K_{P,H2} = \left(\frac{K_{P,H2O} \cdot K_{P,gas-phase}}{K_{P,O2}}\right)^{\frac{1}{2}} \quad [9]$$

$$\Delta H_{H2}^\circ = \frac{\Delta H_{gas-phase}^\circ + \Delta H_{H2O}^\circ - \Delta H_{O2}^\circ}{2} \quad [10]$$

$$\Delta S_{H2}^\circ = \frac{\Delta S_{gas-phase}^\circ + \Delta S_{H2O}^\circ - \Delta S_{O2}^\circ}{2} \quad [11]$$

To solve the system of Equations ((2), (4), (6) and (8), additional conditions have to be verified at the boundary and inside of the membrane such as:

- Yttrium concentration maintained equal to dopant level:

$$\left[Y'_{X_B}\right]_L + \left(Y'_{X_B} - O_o^{\cdot}\right) = \left[Y'_{X_B}\right]_L^\circ \; with \; \left[Y'_{X_B}\right]_L^\circ = 0.2(BZY) \div 0.15(BCZY) \quad [12]$$

- Conservation of the oxygen sites per formula unit, in a single perovskite lattice, as equal to 3:

$$[V_o^{\cdot\cdot}]_L + [OH_o^{\cdot}]_L + [O_o^{\cdot}]_L + [O_o^x]_L + \left[\left(Y'_{X_B} - O_o^{\cdot}\right)\right]_L = 3 \quad [13]$$

- Electroneutrality condition:

$$2\left[V_o^{\cdot}\right]_L + \left[OH_o^{\cdot}\right]_L + \left[O_o^{\cdot}\right]_L - \left[Y'_{X_B}\right]_L = 3 \quad [14]$$

When the concentration of each defect at the boundary of the membrane is determined according to the local fluids' composition and partial pressures, their motion can be described according to the Nernst-Planck-Poisson (NPP) problem, which is expressed by mass and charge conservation equations. First, the defect conservation inside the membrane can be described by the equation:

$$\frac{\partial[X_k]}{\partial t} + \nabla \cdot J_k = 0 \quad [15]$$

which, in steady state condition, simplifies to $\nabla \cdot J_k = 0$ [12,15,28].

The term J_k represents the flux of a specific defect and can be described by the Nernst-Planck equation as:

$$J_k = -D_k\left(\nabla[X_k] + \frac{z_k F}{RT}[X_k]\nabla\phi_e\right) \quad [16]$$

with D_k [m^2/s] representing the diffusivity of a defect described by the equation

$$D_k = D_k^{\circ} \exp\left(\frac{-E_k}{RT}\right).$$

The term z_k represents the charge of the defects, respectively equal to 1 for protons and polarons and 2 for the oxygen vacancies. Finally, $\nabla\phi_e$ the gradient of the electrostatic potential.

This last term can be related to the local charge density (ρ (C/m^3)) depending on the relative permittivity (ε_r) [33] through the Gauss Law shown in Equation (17).

$$\nabla \cdot (\varepsilon_r \varepsilon_o \nabla\phi) = -\rho = -F\sum z_k[X_k] \quad [17]$$

Both the defect concentration and electrostatic potential at the boundary of the membrane must be defined as boundary conditions for the resolution of the system of equations.

Useful for cell model implementation is also the definition of overall conductivity, defined as the summation of the partial conductivities of each defect, according to the Nernst-Einstein Equation (18).

$$\sigma = \frac{F^2}{RT}\sum_{k=1}^{K} z_k^2[X_k]D_k \quad [18]$$

2.2.2. Thermodynamic parameters estimation for $BaCe_{0.65}Zr_{0.2}Y_{0.15}O_{3-\delta}$ electrolyte material

Thermodynamic parameters, still not available in literature, have been estimated for a new material exploiting experimental data of conductivities with variable steam and oxygen partial pressures for the $BaCe_{0.65}Zr_{0.2}Y_{0.15}O_{3-\delta}$ already available in literature [34]. The selection of this specific composition has been performed since the available experimental data satisfies the requirements for the fitting procedure. Despite this reference already provided partial conductivities, these are not suitable for the NPP model implemented in this work and they also do not allow to determine separately the contribution of the interaction between gas and perovskite and of the diffusivities in the membrane for each ion. Furthermore, no values for the oxygen vacancies have been provided in the paper available in literature [34]. Therefore, enthalpies and entropies have been evaluated minimizing the conductivities estimated through the model, defined by Equation (18) with respect to the experimental ones according to the objective function shown in Equation (19). For this parameter estimation, the trapping effect of polarons with the dopants has been considered.

$$\min\sum_{n=1}^{N}\left(ln(\sigma_{experimental}) - \ln(\sigma_{model})\right)^2 \quad [19]$$

It should be noted that the values obtained are not unique and different combinations provide the same overall conductivities measured experimentally. This problem could be assessed through new tests combining equilibrium and conductivity-relaxation measurements to improve the fidelity of the derived properties [28]. The parameters shown are those related to the best and most reasonable fitting and therefore to the lowest objective function.

Furthermore, the value for ΔH°_{H2O} has been evaluated according to the available correlation to the difference in Allred-Rochow electronegativities between A and B site elements as highlighted in Equation (20) well known and available in literature [35].

$$\Delta H^{\circ} = 400\ \Delta x_{B-A} - 180 \quad [20]$$

Being different dopants present in the B-site of this perovskite (Zr, Ce, Y), a weighted average has been used to account for the cations' electronegativity.

The final values used for the modeling of the electrolyte materials for the state of the art BZY and for the newly extrapolated data for the BCZY have been summarized respectively in Tables 1 and 2.

The derived values show reasonable values also compared to other $Ba(Ce, Zr, Y, Yb)O_{3-\delta}$ oxides available in literature [13,28]. A more detailed discussion is made in the comparison between the derived thermodynamic parameters for defects reaction in the BCZY and those available in literature for the $BaCe_{0.7}Zr_{0.1}Y_{0.1}Yb_{0.1}O_{3-\delta}$ which shows similar cerium and zirconium content, to validate the oxidation enthalpy. The outcome of this comparison shows a slightly more endothermic enthalpy oxidation in the BCZY with respect to the BCZYYb which has a value of +114.88 kJ/mol. The slightly higher endothermic oxidation can be associated also to lower holes concentration due to shallow acceptor level depth [36]and as also confirmed by additional studies available in literature which focus on the effect of yttrium and ytterbium on the defects formation [37].

2.2.3. Thermal modeling

The final modeling approach for this layer involves thermal analysis. The thermal properties of the solid, such as thermal conductivity (k), density (δ) and heat capacity at constant pressure (C_p) are assumed respectively as 2.16 $W/(m \cdot K)$, 452.62 kg/m^3 and 3515.8 $J/(kg \cdot K)$.

This layer is also a heat source, evaluated according to Equation (21), and produced due to the losses associated with its resistivity and to all the ions moving through the membrane.

$$Q_{JH} = ASR \cdot i_{tot}^2 \quad [21]$$

The complete energy conservation equation for this element, in a control volume based formulation, is expressed by Equation (22), with u (m/s) being the velocity vector of translational motion, d_z the characteristic length (m), Q the heat generation rate (W/m^3), q_o (W/m^2) additional heat source and Q_{ted} (W/m^3) additional thermoelectric effects.

Table 1
Thermodynamic parameters for defect reactions with trapping for the electrolyte materials.

Reaction	$\Delta H^{\circ}\left[\frac{kJ}{mol}\right]$		$\Delta S^{\circ}\left[\frac{J}{mol \cdot K}\right]$	
	BZY [15]	BCZY (own calculation)	BZY [15]	BCZY (own calculation)
$\frac{1}{2}H_2 + O_o^{\times} \leftrightarrow OH_o^{\cdot}$	−228.36	−119.27	−54.80	−33.25
$\frac{1}{2}O_2 + O_o^{\times} + V_o^{\cdot} \leftrightarrow 2O_o^{\cdot}$	115.31	+132.57	−45.89	−119.93
$H_2O + V_o^{\cdot} + O_o^{\times} \leftrightarrow 2OH_o^{\cdot}$	−93.30	−123.00	−100	−130.95
$Y'_{X_B} + O_o^{\cdot} \leftrightarrow (Y'_{X_B} - O_o^{\cdot})$	−90.30	−35.36	−6.71	105.65
$H_2 + \frac{1}{2}O_2 \leftrightarrow H_2O$	−248.11		−55.48	

Table 2
Diffusion coefficients of the defects with trapping for the electrolyte materials.

Defects	$D_k^\circ\left[\frac{m^2}{s}\right]$		$E_k^\circ\left[\frac{kJ}{mol}\right]$	
	BZY [15]	BCZY (own calculation)	BZY [15]	BCZY (own calculation)
$OH_o^\cdot$	$5.18\cdot 10^{-7}$	$1.63\cdot 10^{-7}$	60.66	47.19
$V_o^\cdot$	$2.03\cdot 10^{-7}$	$1.36\cdot 10^{-7}$	85.19	68.06
$O_o^\cdot$	$1.38\cdot 10^{-5}$	$2.50\cdot 10^{-3}$	7.18	9.73

$$d_z\rho C_p u\cdot\nabla \mathrm{T}+\nabla\cdot(-d_z k\nabla \mathrm{T})=d_z Q+q_o+d_z Q_{ted} \quad [22]$$

2.3. Gas ducts and interconnects

In the gas channel domains, this paper employs a mixed-gas feed consisting of hydrogen and nitrogen on the cathode, and steam and air on the anode with compositions at the inlet modified during the various case studies in this work, particularly in terms of water content.

The cathode stream acts solely as a sweep gas to remove produced hydrogen, and the anode stream provides the necessary reactant water for the splitting reaction to occur.

2.3.1. Fluidic model

The model assumes fluid flow occurs in open regions, allowing for the definition of velocity field components in two dimensions (u, v) [m/s] and pressure (p) [Pa]. The governing equations in this domain include Navier-Stokes equations to describe momentum conservation for Newtonian fluids in the channel and mass conservation, expressed by the continuity equation.

The model considers temperature, composition, and pressure-dependent fluid properties, such as density and viscosity, determined using the Peng-Robinson equation of state for the gas phase. The flow within the channels is considered compressible due to limited speed inside the channel, with atmospheric pressure and temperature serving as reference conditions. A no-slip boundary condition is applied at the interconnector walls, contrasting with the membrane wall at the interface with the electrode, described in the following section. In addition to the Navier-Stokes and mass conservation equations, the Maxwell-Stefan diffusion is implemented to model the motion of gas phases in the gas duct. Furthermore, the model includes electric and thermal components. From an electrical perspective, equipotential to the imposed voltage is considered, assuming negligible electrical resistance.

2.3.2. Thermal model

The thermal model considers energy balance and simplified heat transfer equation:

$$\rho C_p \mathrm{u}\cdot\nabla \mathrm{T}+\nabla\cdot q=Q \quad [23]$$

With q [W/m^2] heat flux and Q [W/m^3] additional heat sources. The fluid's thermal conductivity, density, heat capacity, and the ratio of specific heats, as previously introduced, are defined considering a real fluid according to the Peng-Robinson model.

2.4. Electrodes

2.4.1. Electrical and ionic conduction model

These layers can be depicted as porous media, allowing gas transport toward the membrane. First, the gas diffusion layer, essential for the flow of electricity and fluid, is established followed by the gas diffusion electrode where the electrochemical reactions are also occurring. Within these domains, the conservation of charge, outlined by Ohm's law in Equation (24), and the charge balance shown in Equation (25) are considered:

$$i=-\sigma_{s,eff}\nabla\Phi_e \quad [24]$$

$$\nabla\cdot \mathrm{i}_s=-i_{v,tot} \quad [25]$$

Within these equations $\sigma_{s,eff}$ represents the effective electronic conductivity, assumed to be 10000 S/m, while $i_{v,tot}$ (A/m^3) indicates the overall volumetric current density due to the electrode reactions and is assumed as null in the GDL.

The GDE is also characterized by additional physics, including the introduction of electrolyte conductivity. The effective conductivity value is lower than that in the membrane and is defined by a correction factor, which depends on the electrolyte volume fraction in the active phase. This factor is assumed to be 0.4 for both electrodes [38].

The most relevant difference though, as mentioned above, is the introduction of the oxidation and reduction reactions at the two sides. The first meaningful parameter is the cell voltage in equilibrium condition, valid in open circuit voltage, which only depends on the Gibbs free energy of the reaction and on the partial pressure of the reactants and products according to the equation, in electrolysis mode with a $\Delta g_{reaction}>0$:

$$E_{eq}=\frac{\Delta g_{reac}(t,p_i)}{zF}=-\frac{\Delta g_{reac}(t,p_0)}{zF}-\frac{\mathrm{RT}}{zF}ln\frac{\prod_R\left(pi/p_0^{v_i}\right)}{\prod_P\left(pi/p_0^{v_i}\right)} \quad [26]$$

The second term introduced is the activation overvoltage, defined as $\eta=E_{ct}-E_{eq}$ with

$E_{ct}=\Phi_s-\Phi_l$ difference between electrode and electrolyte electrostatic potential. This parameter is connected to the charge transfer in both electrodes and therefore to the kinetic of the reaction and to its kinetic law.

The approach used considers the Butler-Volmer kinetic expression which is:

$$i_{loc}=i_0\left(\exp\left(\frac{\alpha_a F\eta}{RT}\right)-exp\left(\frac{-\alpha_c F\eta}{RT}\right)\right) \quad [27]$$

with α_a and α_c respectively anodic and cathodic transfer coefficient and i_0 the exchange current density, characteristic of the open circuit condition.

The electrode reaction source and the local current are finally linked to one another through the active specific surface area considered to be equal to 10^9 1/m.

2.4.2. Fluidic and thermal model

The gas transport considers the gas diffusivity through a porous medium with a gas pore volume fraction of 0.4, used to evaluate the correction factor (f_g) that multiplies the diffusivity according to the Bruggeman method which uses the equation $f_g=\epsilon_g^{1.5}$. A permeability of 10^{-10} m^2 is assumed. The flow model considered in the porous medium is a Darcian flow where conservation of mass, defined by continuity equation, and considers mass sources or sinks (Q_m).

The equation imposed in this domain, when the inertial terms are considered, is the Stokes-Brinkman equation in a porous media.

Inside of the electrode, heat is also produced due to irreversibility compared to the ideal reaction.

2.5. Model calibration and validation

The calibration of the model is performed using data and measurements available from literature for a cell with structure Ni-BZY|BZY|SFM-BZY [32]. While SFM is not an optimal anode material, its selection was driven by the relevance of experimental data rather than its performance. The reference was chosen primarily for its electrolyte

material, for the experimental data in electrolysis mode, the comparison between BZY and BCZY cathodes, along with multiple information for validation like open circuit voltage, transport number and faradaic efficiency.The chemical composition for the BZY and SFM are respectively $BaZr_{0.8}Y_{0.2}O_{3-\delta}$ and $Sr_2Fe_{0.15}Mo_{0.5}O_{6-\delta}$. The geometry of the cell used for the calibration has already been shown in Fig. 1-a. The calibration has been performed with two extreme operating temperatures provided in the reference, considering 80 % N_2 – 20 % H_2 and 3 % H_2O + Air, respectively as cathodic and anodic streams, and a validation with the intermediate one has been performed. Validation has also been performed by comparing the modeled faradaic efficiency, a fundamental key performance indicator for this technology, with the ones provided in the reference and with other similar materials available in literature [13, 34].

Another parameter used for validation is the open circuit voltage (OCV), for which modeled and experimental values have a discrepancy lower than ±2 % as shown in Table 3. The values provided have been evaluated in this model by imposing the overall electrode current density as equal to zero and calculating the OCV as the difference between the electrode potential on the surface of the two electrodes, resulting as equipotential surfaces (i.e. average potential on the electrode surface equal to local potential), that provides this condition. The final validation is also performed through a comparison of the transport number of ions at OCV shown in Table 3 and defined through ionic and electronic resistances [39]. The relationship between OCV, Nernst and transport number agrees with what has been defined in literature [40].

The exchange current densities defined from calibration data from a button cell have been maintained during the various simulations.

The variables have mostly been assessed through average values on the domain, horizontal and vertical cut lines.

2.6. Sensitivity analysis

The calibrated model is finally used to extrapolate the results, in terms of performance, focusing on the effect that different operating conditions have mainly on the polarization curve, internal temperature profile, transport number at the OCV and faradaic efficiency.

This evaluation is performed by acting on two main operating conditions which are operating temperature and gas composition at the inlet of each electrode.

Concerning the temperatures, the impact of operating temperatures of 550 °C, 600 °C and 650 °C on the most important parameters of the cell, such as current leakage or voltage gradients, are assessed.

Regarding the composition, mainly the impact given by the humidification is provided by focusing on water content respectively on the cathode or on the anode. The gas fed assumed for the sensitivity analysis are respectively 10 %-30 %-50 % H_2O + remaining N_2+H_2 (4:1 ratio) at the cathode side and 30 %-60 %-90 % H_2O + Air at the anode. It is important to clarify that degradation and negative effects on the chemical and mechanical stability of the membrane that may derive from high water contents are here neglected.

3. Results and discussion

The results obtained from each sensitivity analysis are introduced in the following sections.

Table 3
Open circuit voltage baseline validation.

Temperature [°C]	Experimental OCV [V]	Experimental transport number [−]	Model OCV [V]	Model transport number [−]
550	0.948	0.967	0.960	0.966
600	0.921	0.942	0.916	0.949
650	0.894	0.916	0.879	0.936

3.1. Temperature sensitivity

In this section, the effect of different operating temperatures is assessed by showing some of the most relevant performance indicators (e.g. polarization curves, transport number at OCV, current densities for each ion and related faradaic efficiency, voltage and ions distribution within the membrane).

During this evaluation, the gas composition at the inlet of both electrodes is set to dry 80 % N_2+20 % H_2 at the cathode side and 30 % H_2O + Air at the anode. The temperature of the fluids at the inlet, instead, is fixed to the operating temperature of the cell. The first result, as highlighted by the polarization curve in Fig. 2-a, confirms the positive effect of the higher temperature on the overall performance. The lower temperatures will present a higher slope of the curves and therefore higher area specific resistances (ASR) and consequently worse performance. But the temperature affects in different ways multiple defect conduction.

As depicted in Fig. 2-b and 2-c, both proton and electron hole conductivities exhibit an increase with rising temperatures, mainly due to the enhanced diffusion and mobility of defects within the membrane. However, a distinction in the sensitivity of their diffusivities can be observed, especially at higher applied voltages, which increase the electrolyte potential gradient across the membrane. Since the diffusivity of electron holes exhibits a stronger temperature dependence compared to protons as well as showing higher absolute values, an increase in the potential gradient has a more pronounced effect on electron hole transport especially since the diffusivity term is directly multiplied by the potential gradient in the Nernst-Planck equation, leading to an amplified contribution of electron holes to the overall ionic flux at elevated voltage gradients. Consequently, while the i-V curves for protons maintain a relatively uniform spacing across the voltage range at different temperatures, the curves for electron holes diverge more prominently at higher voltages, since the electrochemical heating of the cell further increases the operating temperature, reflecting also their heightened sensitivity to thermal and electrical driving forces.

To better assess the effect of temperature, the transport number is also evaluated at the OCV, providing values at 550,600 and 650 °C respectively equals to 0.970,0.957,0.948.

From the faradaic efficiency, defined as $FE = \frac{J_{OH^-_a}}{|J_{ext}|}$ shown in Fig. 2-d, two main trends can be highlighted: one associated with the operating voltage and one with the temperature. Regarding the first, we observe that higher voltages, which are also associated with higher current densities, negatively impact the FE, especially when higher operating temperatures are employed. The higher current densities have a double impact, one on the ions concentrations through the membrane and another on the heating of the cell. The change in ions trend affects, according to Equations (16) and (18), both diffusivity due to gradient variation ($\nabla[X_k]$) and migration due to change in absolute value ($[X_k]$), but this has a minimal effect on the transport number and faradaic efficiency.

The primary explanation lies in the non-isothermal nature of the cell behavior within the model, which results in spatially non-uniform operating temperatures, higher than the gas inlet temperature, that has been imposed constant during the simulation of cell operation. This temperature increase, driven by electrochemical heating, has the same effects that can be deduced by the temperature sensitivity analysis, attributed to the different transport mechanisms of protons and electron holes, as previously discussed, which also cause the voltage corresponding to the maximum faradaic efficiency to shift. At higher temperatures, this maximum occurs at lower applied voltages due to a reduced difference in the electric migration contribution between holes and protons fluxes. A more detailed explanation is provided by the temperature-dependent variation in proton concentration at the membrane boundaries and within the membrane, as illustrated in Fig. 2-e. Increased temperatures lead to reduced membrane hydration, which in

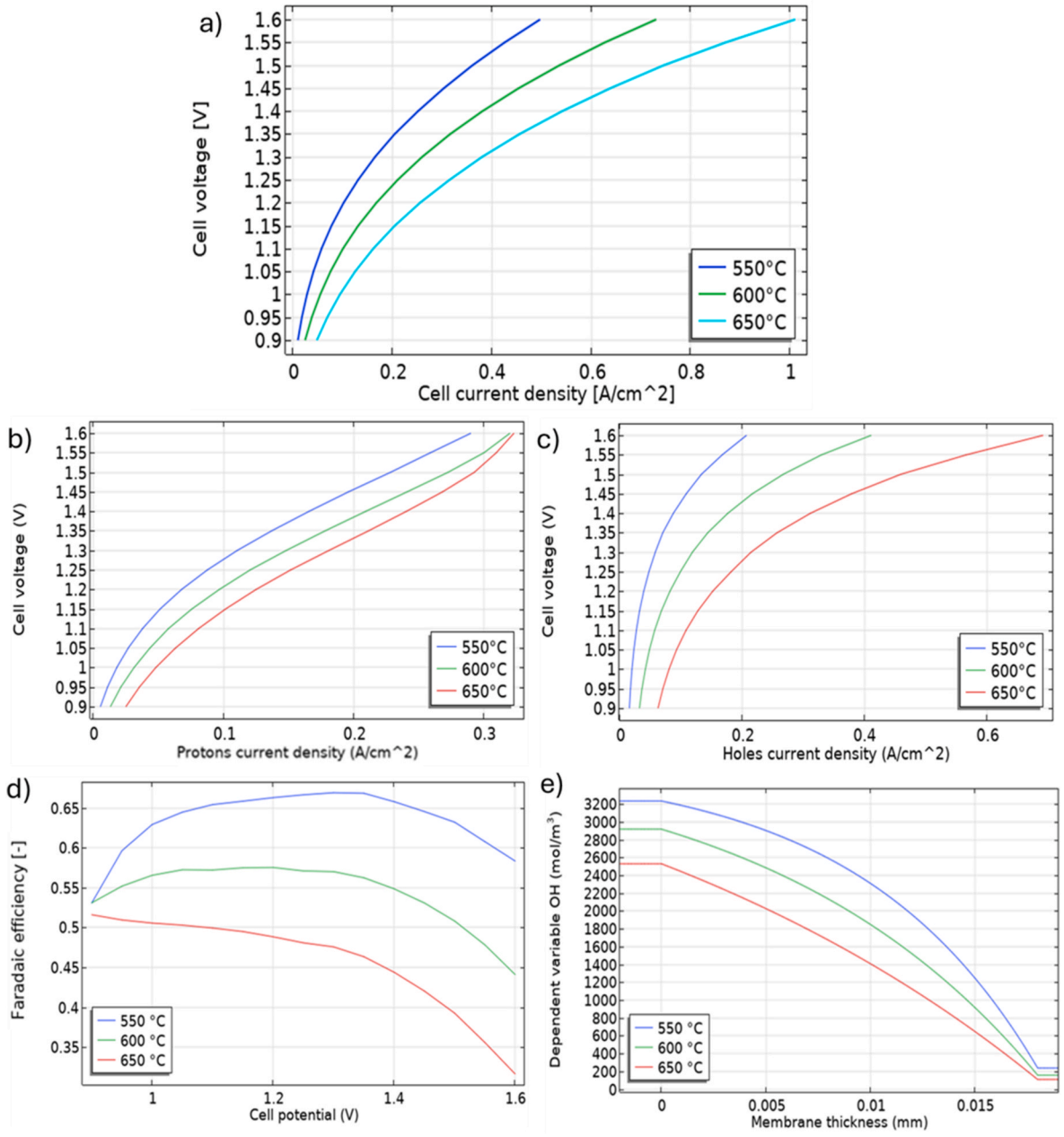

Fig. 2. Polarization curves considering (a) all defects (b) protons (c) electron holes, (d) faradaic efficiency, (e) protons defects in the membrane; depending on operating temperature.

turn lowers the proton concentration. This reduction affects the ionic concentration gradients within the membrane, impacting directly on the diffusion and indirectly influencing the migration contribution to the ionic fluxes.

The change of gas composition in the air side between the calibration condition, at 3 %, and the current case study at 30 %, also impacts the open circuit voltage value.

In Fig. 2-a lower values of OCV are observed, compared to those provided in the calibration shown in Table 3. This change in OCV occurs since atmospheric conditions have an impact, and in particular, higher water content at the air side tends to decrease it [41,42], bringing the values close to other results available in literature, where BZY20 is also used in electrolysis mode [43].

Additional results, obtained from the thermal and fluidic model, are presented to assess the temperature distribution within the cell. Specifically, the temperature distribution at an intermediate value of 600 °C at thermo-neutral and maximum operating voltage of 1.6 V, respectively shown in Fig. 3-a and 3-b. These results are consistent with other operating temperatures, with differences primarily in the absolute temperature values.

Several key observations can be made regarding the temperature distribution. If the thermo-neutral operation shows uniform temperature distribution throughout the cell, since the heat produced is consumed for the electrochemical reaction, more interest can be given to the operation at 1.6 V.

First, the temperatures inside the cell can reach up to 45 °C higher than the theoretical operating temperature. This effect is particularly pronounced on the right half of the cell and can be attributed to multiple factors.

One key contributor is the inlet temperature of the fluid streams, which is maintained at the operating value. As a result, the fluid serves primarily as a reactant rather than a coolant, leading to a buildup of heat

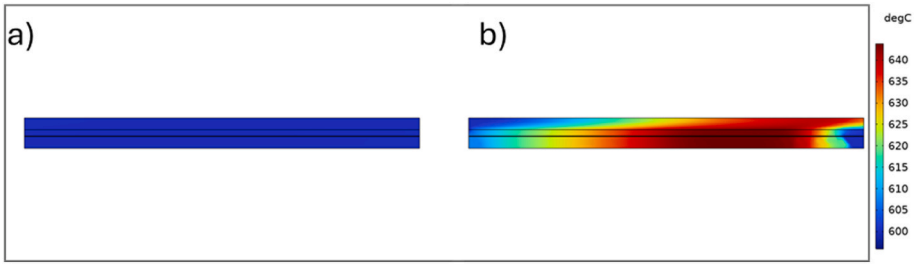

Fig. 3. Temperature distribution inside of the cell at 600 °C operating temperature and at a) thermo-neutral voltage b) cell potential of 1.6V

within the channels and a corresponding temperature rise. On the anode side, the temperature initially increases and then decreases as the fluid moves downstream, primarily due to the cooler cathode-side stream.

This temperature behavior is also influenced by the distribution of reactants within the cell, which is linked to the counter-flow configuration employed. The cathodic inlet is located at the top left of the cell, while the anodic inlet is at the bottom right. Consequently, the current density distribution within the membrane is not uniform, with the maximum current density coinciding with the regions of the cell where the highest temperatures are observed.

Changes in the flow rate at the two channels and especially in the streams' temperature at the inlet could also therefore affect the temperature distribution, but it is not further studied and deepened in this work.

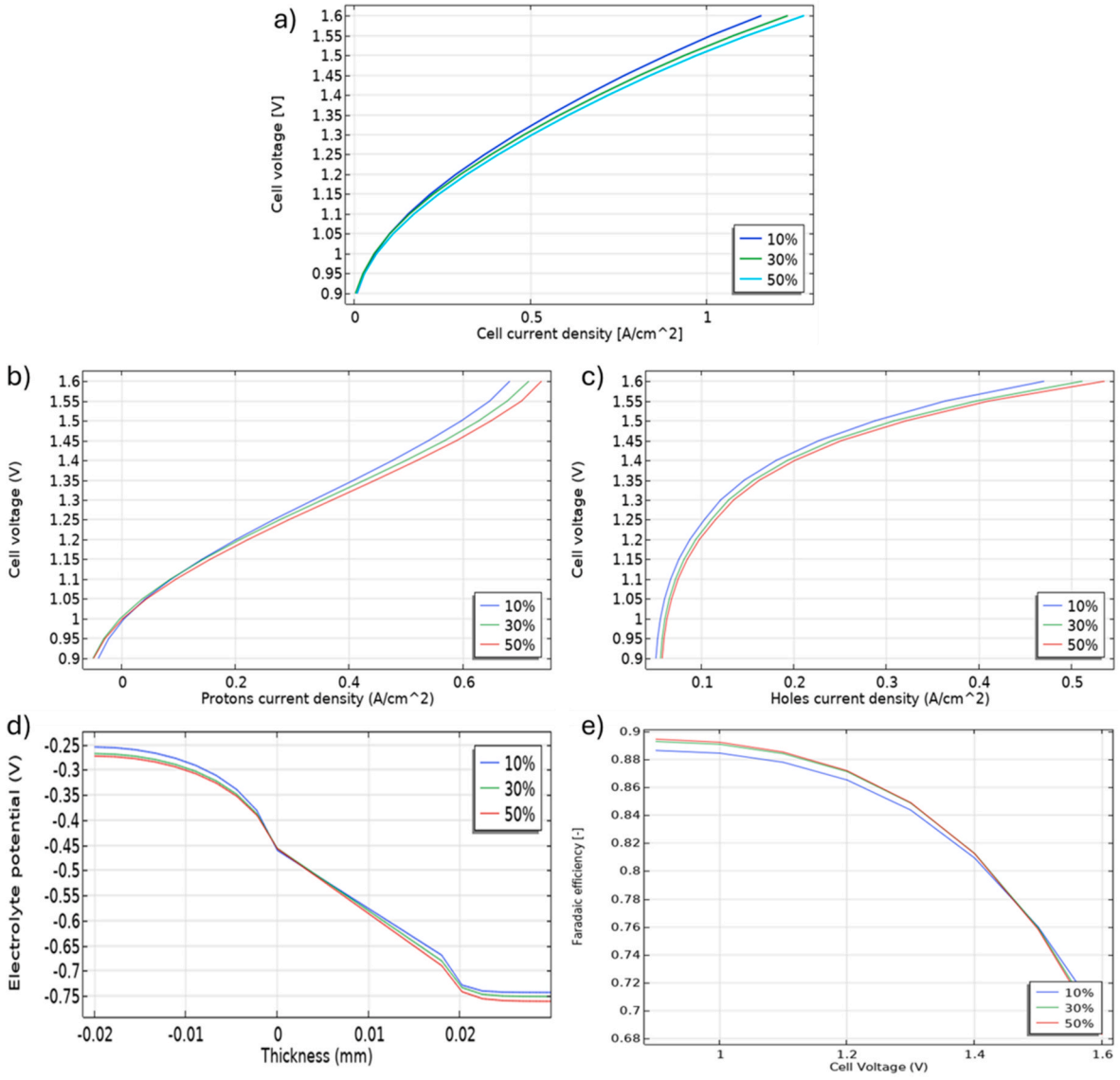

Fig. 4. Polarization curves considering (a) all defects (b) protons (c) electron holes, (d) voltage profile, (e) faradaic efficiency; depending on water content at the cathode side at 600 °C.

3.2. Water content sensitivity

In this section, the effect of the various inlet stream humidification levels on the overall performance of the cell is presented. The temperature is kept constant to a value of 600 °C.

The main indicators used for the assessment of the performance, similarly to the previous section, are polarization curves, voltage profiles through electrodes and electrolyte, current density for the main defect and faradaic efficiency and corresponding contribution on the overall current density.

3.2.1. Cathode sensitivity analysis

In this section, only the water content at the inlet of the cathode is modified by keeping the anodic one to a constant composition of 90 % H_2O-10 %Air, the use of values this high will have an impact on the sensitivity of the cathode gas composition, specifically reducing it.

It is important to note that the final aim of his study is not related to practical implications, except for some limited application in hydrogen pumping, but it is focused on understanding the impact of humidity on the membrane conductivity, specifically assessing how different hydrogen ions could influence the diffusion term in the Nernst-Planck equation. As shown in Fig. 4-a, an increase in the humidification affects the slope of the polarization curve, leading to lower current densities for a given operating voltage, which can be attributed to multiple phenomena such as changes in voltage profile and defects concentrations.

Firstly the transport number at OCV for water content at the cathode side of 10 %–30 %-50 % reach almost unitary value, especially when higher water contents are used thanks to the combined effect on the Nernst voltage, OCV and OH concentrations, showing, just like for the performance indicators, an improvement when higher water content at the cathode are used.

There is also the effect associated to the change in the voltage profile, shown in Fig. 4-d, due to variation in the partial pressures of the hydrogen, which shifts from a minimum of 1855 Pa with a 50 % water content up to a maximum of 2243 Pa when 10 % humidification is used.

This variation arises from the definition of the hydrogen content at the inlet, calculated as $0.2(1,-x_{H2O})$ which alters the equilibrium voltage at the cathode. The main effect is, therefore, the change in the equilibrium voltage at the hydrogen electrode side, which can be explained by looking at Equation (26), and has values that move from 0.7838 V with 10 % up to 0.791 V when 50 % water content is used. The increase in the equilibrium voltage at the cathode side, combined with the constant value maintained at the anode side, results in higher voltage gradient through the membrane as represented by the slope in Fig. 4-d. This voltage profile is also derived from the overpotential, which decreases as the water content increases.

One of the most impacting elements, though, is linked to the change is the concentration of the defects, according to Equations [1-8] with the corresponding change in flux through the membrane. This is shown by the ions' concentration through, and especially at the boundary, but also by looking at the change in the current density linked to the protons and to the holes.

As depicted in Fig. 5, an increase in the water content will enhance the hydration of the membrane, therefore increasing the protons concentration (OH_o). Although the decrease in hydrogen partial pressure slightly reduces the proton concentration, the equilibrium constants of the competing reactions favour proton production, resulting in a net increase in defect concentration.

Hence, there is a decrease in the gradient of the protons between the two sides of the membrane.

Therefore, even though the diffusion driven protonic flux, which depends on protons concentration differences, is diminished, the migration term, directly associated with the voltage gradient, is favored due to its increase, as previously explained. Hence, the overall current density connected to the protons is increasing, as represented in Fig. 4-b. A similar explanation applies to the electron holes flux, again represented in Fig. 4-c, with differences in terms of absolute values and trends due to the different diffusivities.

The different behavior of the two defects, when water content is changed, can also be summarized by the faradaic efficiency shown in Fig. 4-e which follows similar trend depending on the cell voltage as already previously described.

The low sensitivity of the performance is also emphasized according to studies in literature focused on hydrogen separation and electrochemical hydrogen pumping (EHP) [44].

The results presented here align with these observations, reinforcing the notion that humidification effects on membrane transport must be carefully managed in practical electrochemical applications.

3.2.2. Anode sensitivity analysis

For this study, the sweep gas composition at the cathode inlet of the stack is maintained as equal to dry 20 % H_2 + 80 % N_2.

Firstly the transport number at OCV for water content at the anode side of 30 %–60 %-90 % are calculated and are respectively equals to 0.957,0.962,0.966 at 600 °C.

Firstly an increase in the water content at the anode inlet will improve the i-V curve, as shown in Fig. 6-a. This improvement is

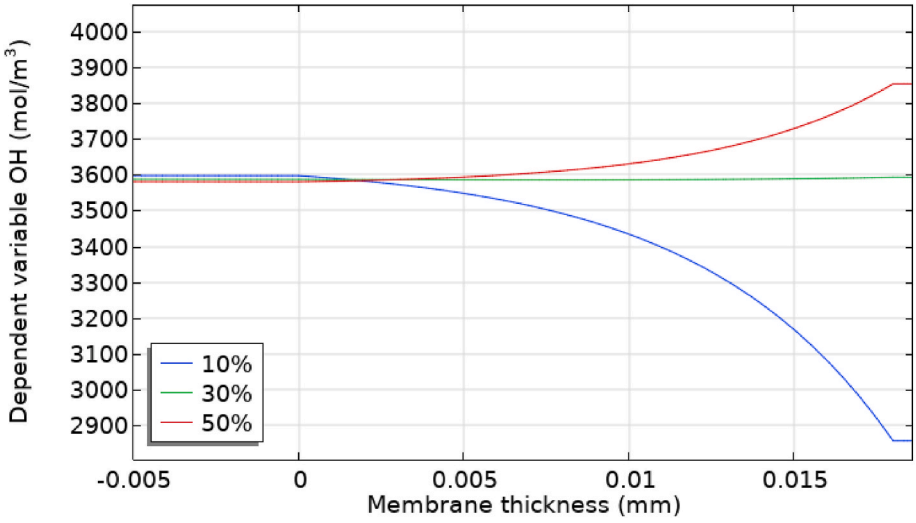

Fig. 5. Protons defects in the membrane depending on water content at the cathode side at 600 °C.

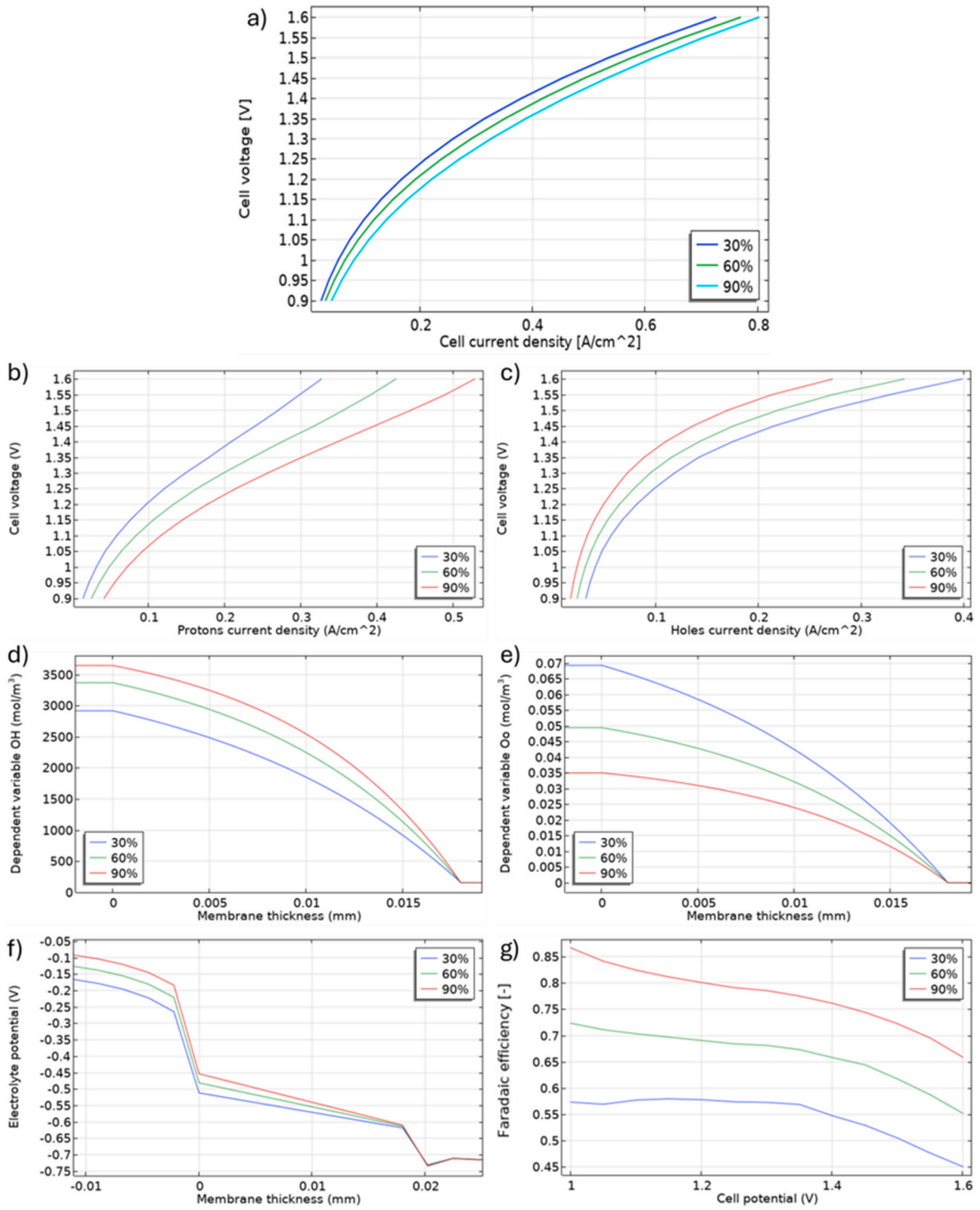

Fig. 6. Polarization curves considering (a) all defects (b) protons (c) electron holes, (d) protons concentration along the membrane, (e) electron holes concentration along the membrane (f) voltage profile (g) faradaic efficiency; depending on water content at the anode side at 600 °C.

attributed to the enhanced water availability, which serves as a reactant in the electrochemical reaction, leading to increased equilibrium voltage and reduced polarization losses.

Most of the observed advantages, though, originate from the change in the defects concentration at the boundary (Fig. 6-d and Fig. 6-e) for both protons and electron holes. The increase in water content, and consequently its partial pressure, raises the concentration of protons at the air electrode side according to hydration reaction from Equation (6), while simultaneously reducing the concentration of holes as described in Equation (4). This second effect can be explained by the decrease in the partial pressure of oxygen at the anode inlet, calculated as $0.21(1 - x_{H2O})$, due to the increase of water concentration.

As already introduced in section 3.1 and as further validated in this sensitivity analysis, higher water content at the air side tends to decrease the open circuit voltage.

The redistribution of defects' concentrations at the boundary, and therefore also of their profiles inside of the membrane, has two consequences. Firstly, it raises the current density associated with the protons

therefore increasing hydrogen production. Furthermore, it also lowers the electron hole contribution to the charge transfer further decreasing the current leakage.

If in the previous sensitivity analysis, there is a tradeoff between the diffusion and the migration, as in this study both of them contribute favorably to the performance of the cell due to higher defects and voltage gradient across the membrane, as shown in the voltage profile of Fig. 6-f. This stronger driving force enhances charge carrier mobility, further improving proton conduction.

This aspect is also further highlighted in the plot representing the faradaic efficiency (Fig. 6-g) which follows similar voltage relation than the previous case studies. Not only does a higher water content allow for a greater maximum faradaic efficiency, but it also shifts the voltage at which this maximum is attained towards lower voltages. This behavior derives from different defect diffusivity and mobility which alter the relative contributions of protons and electron hole on the overall charge transport mechanism.

Therefore it can be concluded, regarding this operating parameter, that higher humidification improves the performance of the cell. However, this improvement must be weighed against potential stability concerns, particularly for electrolyte materials containing ceria, which are known to exhibit degradation under high-humidity conditions. This highlights the need for careful optimization of operating conditions to balance performance gains with long-term durability considerations.

3.3. Comparison between trapping and no trapping assumption

As already mentioned in Section 1, different approaches have been used in literature to model the membranes with one of the main differences being the consideration or not of the trapping effect between polarons and dopant materials highlighted in Equation (7). Despite in literature, several studies have tried to assess the effect that this assumption has on membrane behavior and performance [13,15], a gap in literature has been found in the assessment on the effect that these two different modeling approaches have on the overall electrochemical performance of fuel-cell, and electrolyzers as in this case, when also electrodes are included.

Therefore, in this section, the thermodynamic parameters for gas-perovskite interaction and the values for the diffusivities typically used for BZY with trapping, have been instead substituted with the ones fitting neglecting this interaction between electron holes and dopant, as presented in available literature [15]. The assumptions regarding electrodes and the remaining elements of the cell have been maintained the same. The results are obtained with temperature values of 550 °C, 600 °C and 650 °C while maintaining the stream compositions at the inlet of 80 % N_2+20 % H_2 at the cathode side and 30 % H_2O + Air at the

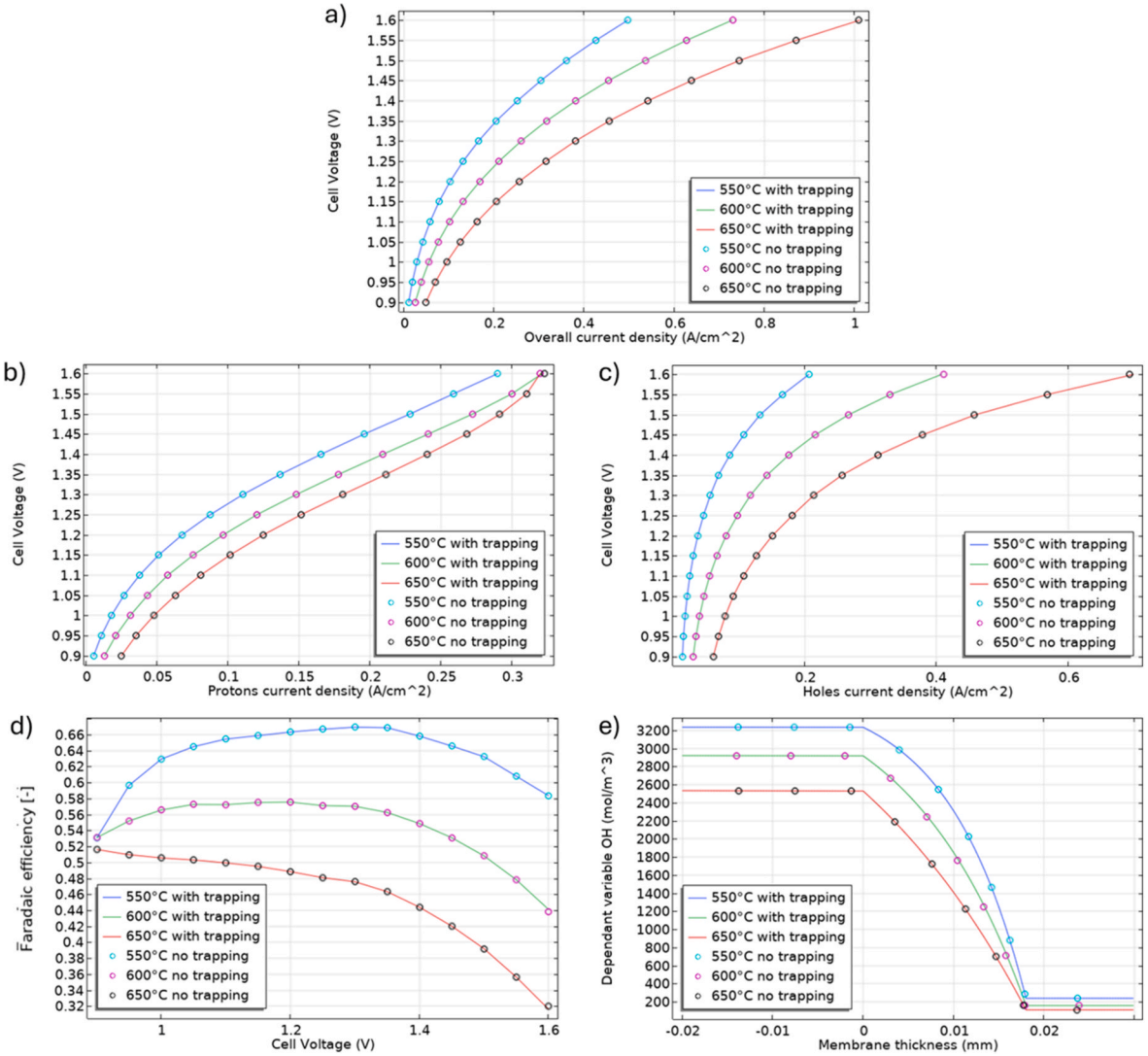

Fig. 7. Polarization curves considering (a) all defects (b) protons (c) electron holes, (d) faradaic efficiency (e) protons defects in the membrane; comparison between trapping and no trapping with BZY electrolytes.

anode used already in section 3.1.

The results, summarized in Fig. 7, show that the overall electrochemical performance of the cell remains unaffected by the inclusion or exclusion of the trapping with no significant deviations between the two assumptions. This also aligns with other findings which suggested that, although trapping reduces the concentration of mobile electron holes, the electrochemical performance is mitigated by changes in their diffusivity [15]. Other ions, such as the hydrogen one, instead are not affected as also highlighted in Fig. 7-e.

These findings confirm and align with prior research [13,15] and it highlights that, despite the different assumptions also in terms of the fundamental behavior of the perovskite on an ionic point of view, the overall electrochemical performance remains robust despite differences in the microscopic description of polaron transport. This can be in part justified especially when considering that these thermodynamics parameters, summarized in 2.2, are extrapolated by optimization and fitting to the overall conductivity of the electrolyte and have been found to have similar values for the objective functions regardless of whether trapping is included or not. Therefore, it can be confirmed and concluded that this assumption is not critical in terms of performances on a macroscopic basis, the impact on other aspects could be assessed.

3.4. Comparison between $BaZr_{0.8}Y_{0.2}O_{3-\delta}$ and $BaCe_{0.65}Zr_{0.2}Y_{0.15}O_{3-\delta}$

In this final section, the novel electrolyte material has been used as a substitute for the BZY predominantly used in almost all the models available in literature. To compare the two electrolyte materials in terms of overall performance and leakage, the thermodynamic parameters for gas-perovskite interaction and the diffusivities of ions for the BZY electrolyte material have been substituted with those of the BCZY. For both, values are summarized in Tables 1 and 2. The results are shown for temperatures of 600 °C, 650 °C and 700 °C, higher than previous sections since the thermodynamic parameters for the BCZY have been fitted using experimental data from this higher range. Stream compositions at the inlet of 80 % N_2+20 % H_2 at the cathode side and 30 % H_2O + Air at the anode used already in sections 3.1 and 3.3.

The transport number for BZY20 at OCV has already been previously introduced. For the new BCZY, respectively at 600,650 and 700 °C, it corresponds to 0.99, 0.987,0.981.The first key observation from Fig. 8-a, is associated with the current density obtained when considering all of the defects and highlights a trend of the polarization curves at different temperatures similar to the one that could be derived from a direct comparison of the experimental conductivities [34,45]. This result further emphasizes the significance of bulk electrolyte conductivity as a

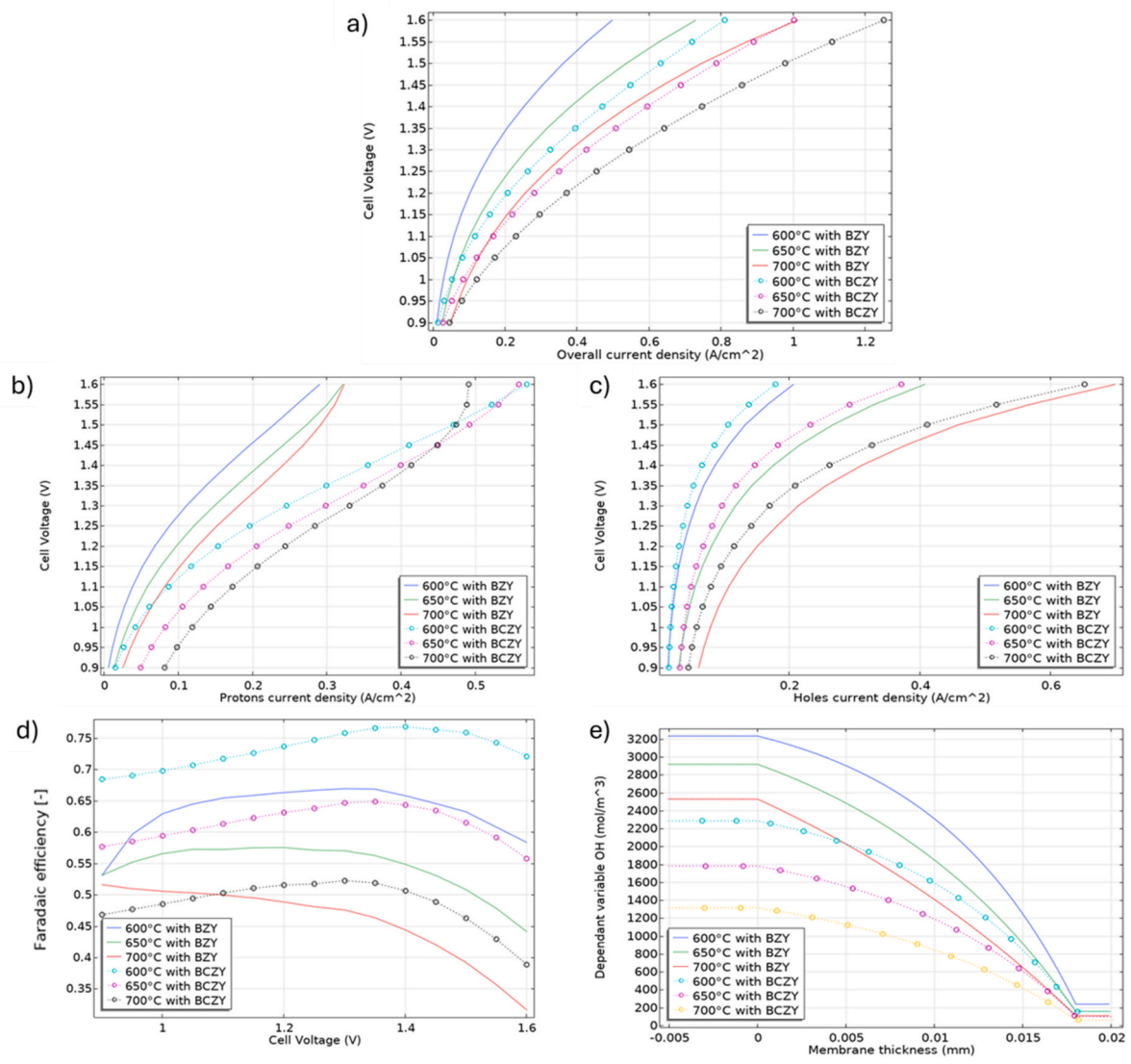

Fig. 8. Polarization curves considering (a) all defects (b) protons (c) electron holes, (d) faradaic efficiency, (e) protons defects in the membrane; comparison between BZY and BCZY at different temperatures.

macroscopic indicator of the electrochemical cells performances. Another noteworthy is deduced from the increasing gap between the two electrolyte materials when lower temperatures are reached and since the PCC technology is typically operated at lower temperatures, this would give further advantages to the BCZY which performs better at 600 °C. The benefit of using BCZY is intensified when considering the difference in protons and electron holes current densities with the related effect on the transport number and faradaic efficiency. The BCZY electrolyte exhibits higher protons current densities (Fig. 8-c) and lower electron holes ones (Fig. 8-b) across all investigated temperatures. The corresponding faradaic efficiency (Fig. 8-d) is consequently characterized by more uniform and higher values, with the maximum values for the BCZY higher than BZY at every temperature indicating improved selectivity toward proton conduction. Also, the voltage value corresponding to the maximum faradaic efficiency is shifted to higher values, likely due to differences in ion diffusivities and the increased influence of the electric field on charge transport mechanisms. Another interesting conclusion is related to the peculiar trend in proton current density at higher voltages, as highlighted in Fig. 8-c, which sees a slight crossing between the polarization curves at 600 °C and 650 °C. This phenomenon can be explained by focusing on the conductivity of these ions and especially on the interplay between concentration, diffusivities and temperature. This parameter is especially important for the indirect effect that it has on others. While an increase in operating voltage, in fact, is mainly related to the increase in the cell temperature due to heat generation in the cell, which enhances protonic diffusivity (D_{OH}) and of decreasing the protons concentration at the gas-perovskite interfaces (OH), respectively with positive and negative effects on the conductivities. This last contribution, more in detail, is the one having the highest sensitivity, leading to an overall decrease in conductivity and to the trend shown. This effect of the temperature on the concentration of protons is also highlighted in Fig. 8-e where lower values for BCZY compared to BZY are spotted. This behavior is strongly dependent on the entropy of hydration (ΔS°_{H2O}). Lower entropy values lead to higher proton concentrations when lower values are obtained in the fitting procedure. Often higher entropy is compensated for by higher diffusivity, leading to similar macroscopic outcomes.

Overall, these results suggest that BCZY is a promising alternative to BZY, offering enhanced protonic transport, lower electron hole leakage, and improved faradaic efficiency. The trend with the voltage is different between BZY and BCZY due to the different sensitivity of diffusivities and gas-perovskite equilibrium reactions to the electrochemical heating. However, its performance advantage at lower temperatures should be weighed.

4. Conclusions and outlook

The main findings deriving from this study regarding the effect of different operating conditions on hydrogen production performance, single defects current densities and related electronic leakage in the Protonic Ceramic Electrolysis Cell (PCEC) can be summarized into the following.

The model developed allowed the assessment of electronic leakage and its influence on the transport number at the OCV and faradaic efficiency at different operating voltages in the PCEC, providing useful insights into the efficiency and performance limitations of the electrolysis process, and highlighting the importance of minimizing electronic leakage for optimal hydrogen production in the PCEC.

Higher operating temperatures, in the range 550 °C–650 °C were found to have a positive effect on the overall performance of the PCEC. Increased temperatures led to improved polarization curves, associated with reduced area specific resistances, while worsening faradaic efficiency due to an increase in the electron holes current higher than the protonic one given the same temperature increase.

Regarding the sensitivity linked to the gas compositions at the inlet of the electrodes, the study focused on the humidification levels at the cathode and anode sides. Water content variations in the gas fed to the electrodes (10 %–50 % at the cathode and 30 %–90 % at the anode) revealed significant effects on the polarization curves, voltage profiles, and current leakage, influencing the hydrogen production efficiency of the PCEC, especially when the anodic stream is modified.

Finally, the newly introduced and studied BCZY electrolyte material has been found to have slightly higher overall current densities, especially at lower temperatures which are optimal for PCC technology, but it has exhibited superior faradaic efficiencies, further highlighting its advantages over the benchmark BZY electrolyte considered.

Overall, the findings emphasize the critical role of operating conditions, such as temperature and gas composition, in determining the hydrogen production performance of the PCEC. Additionally, the consideration of electronic leakage as a factor affecting faradaic efficiency underscores the need for efficient design and operation strategies to enhance the overall performance of protonic ceramic electrolysis cells improving the protonic current while decreasing at the same time the electric holes ones. The design of the cell and its thermal management are also important to remove excess heat produced during the operation which has been demonstrated to affect negatively the cell performances and faradaic efficiency number.

CRediT authorship contribution statement

Andrea Moranti: Writing – review & editing, Writing – original draft, Visualization, Validation, Software, Resources, Methodology, Investigation, Formal analysis, Data curation, Conceptualization. **Domenico Ferrero:** Writing – review & editing, Validation, Supervision, Resources, Project administration, Methodology, Investigation, Formal analysis, Data curation, Conceptualization. **Francesco Da Prato:** Writing – review & editing, Validation, Resources, Methodology, Investigation, Formal analysis, Data curation. **Simone Anelli:** Writing – review & editing, Validation, Supervision, Resources, Methodology, Investigation, Formal analysis, Data curation. **Federico Smeacetto:** Writing – review & editing, Validation, Supervision, Resources, Project administration, Investigation, Funding acquisition, Formal analysis, Data curation, Conceptualization. **Massimo Santarelli:** Writing – review & editing, Validation, Supervision, Resources, Project administration, Methodology, Investigation, Funding acquisition, Formal analysis, Data curation, Conceptualization.

Declaration of competing interest

The authors declare that they have no known competing financial interests or personal relationships that could have appeared to influence the work reported in this paper.

Acknowledgement

This research has received funding from the European Union under grant agreement No 101099717 – ECOLEFINS project, and grant agreement No. 101137802 – ELECTROLIFE project, as well as from UK Research and Innovation (UKRI) under the UK governments Horizon Europe funding Guarantee (10079292). Views and opinions expressed are however, those of the author(s) only and do not necessarily reflect those of the European Union or European Innovation Council and SMEs Executive Agency (EISMEA), the ELECTROLIFE or ECOLEFINS consortia, or UK Research and Innovation granting authorities. Neither the European Union nor the granting authorities can be held responsible for them. We also would like to acknowledge Fondazione Bruno Kessler (FBK) for the exchange opportunities and for funding Andrea Moranti' s PhD, who contributed to this publication.

Abbreviations

ASR	Area specific resistance
BCY	Barium cerate
BCZY	Barium cerium-zirconate ($BaCe_{0.65}Zr_{0.2}Y_{0.15}O_{3-\delta}$)
BZY	Barium zirconate ($BaZr_{0.8}Y_{0.2}O_{3-\delta}$)
EHP	Electrochemical hydrogen pumping
GDE	Gas diffusion electrode
GDL	Gas diffusion layer
HRR	Hydrogen reduction reaction
MIEC	Mixed ion and electronic conductor
NPP	Nernst-Planck-Poisson
PCCs	Protonic ceramic cells
RES	Renewable energy sources
SFM	Molybdenum doped strontium ferrite ($Sr_2Fe_{0.15}Mo_{0.5}O_{6-\delta}$)
SOCs	Solid oxide cells
TCO	Triple conducting oxide
TPBs	Triple phase boundaries
WOR	Water oxidation reaction

Data availability

Data will be made available on request.

References

[1] O.O. Yolcan, World energy outlook and state of renewable energy: 10-year evaluation, Innov. Green Dev. 2 (2023) 100070, https://doi.org/10.1016/j.igd.2023.100070.

[2] M.F. Lagadec, A. Grimaud, Water electrolysers with closed and open electrochemical systems, Nat. Mater. 19 (2020) 1140–1150, https://doi.org/10.1038/s41563-020-0788-3.

[3] S.R. Mendes, G.M.G. da Silva, E.S. Araújo, P.M. Faia, A review on low-temperature protonic conductors: principles and chemical sensing applications, Chemosensors 12 (2024), https://doi.org/10.3390/chemosensors12060096.

[4] S. Cheng, X. Li, X. Huang, Y. Ling, S. Liu, T. Li, Hydrogen separation via proton conducting ceramic membranes: a review, Int. J. Hydrogen Energy 70 (2024) 654–665, https://doi.org/10.1016/j.ijhydene.2024.05.181.

[5] J. Lee, J. Otomo, Proton conduction-assisted direct CO2 methanation using Ni/CaO/Y-doped BaZrO3 proton conductor, Fuel 322 (2022) 124094, https://doi.org/10.1016/j.fuel.2022.124094.

[6] I.T. Bello, S. Zhai, Q. He, C. Cheng, Y. Dai, B. Chen, Y. Zhang, M. Ni, Materials development and prospective for protonic ceramic fuel cells, Int. J. Energy Res. 46 (2022) 2212–2240, https://doi.org/10.1002/er.7371.

[7] C. Duan, R. Kee, H. Zhu, N. Sullivan, L. Zhu, L. Bian, D. Jennings, R. O'Hayre, Highly efficient reversible protonic ceramic electrochemical cells for power generation and fuel production, Nat. Energy 4 (2019) 230–240, https://doi.org/10.1038/s41560-019-0333-2.

[8] K.D. Kreuer, Proton-conducting oxides, Annu. Rev. Mater. Res. 33 (2003) 333–359, https://doi.org/10.1146/annurev.matsci.33.022802.091825.

[9] K.D. Kreuer, St Adams, W. Münch, A. Fuchs, U. Klock, J. Maier, Proton conducting alkaline earth zirconates and titanates for high drain electrochemical applications, Solid State Ionics 145 (2001) 295–306, https://doi.org/10.1016/S0167-2738(01)00953-5.

[10] M.K. Hossain, M.C. Biswas, R.K. Chanda, M.H.K. Rubel, M.I. Khan, K. Hashizume, A review on experimental and theoretical studies of perovskite barium zirconate proton conductors, Emerg. Mater. 4 (2021) 999–1027, https://doi.org/10.1007/s42247-021-00230-5.

[11] A.M. Dayaghi, J.M. Polfus, R. Strandbakke, A. Pokle, L. Almar, S. Escolástico, E. Vøllestad, J.M. Serra, R. Haugsrud, T. Norby, Effects of sintering additives on defect chemistry and hydration of BaZr0.4Ce0.4(Y,Yb)0.2O3−δ proton conducting electrolytes, Solid State Ionics 401 (2023) 116355, https://doi.org/10.1016/j.ssi.2023.116355.

[12] H. Zhu, R.J. Kee, Membrane polarization in mixed-conducting ceramic fuel cells and electrolyzers, Int. J. Hydrogen Energy 41 (2016) 2931–2943, https://doi.org/10.1016/j.ijhydene.2015.10.100.

[13] H. Zhu, S. Ricote, C. Duan, R.P. O'Hayre, R.J. Kee, Defect chemistry and transport within dense BaCe0.7Zr0.1Y0.1Yb0.1O3 − δ (BCZYYb) proton-conducting membranes, J. Electrochem. Soc. 165 (2018) F845, https://doi.org/10.1149/2.1091810jes.

[14] F.W. Poulsen, [Equations solution method] method for calculating ionic and electronic defect concentrations in proton containing perovskites, J. Solid State Chem. 143 (1999) 115–121, https://doi.org/10.1006/jssc.1998.8092.

[15] H. Zhu, S. Ricote, C. Duan, R.P. O'Hayre, D.S. Tsvetkov, R.J. Kee, Defect incorporation and transport within dense BaZr0.8Y0.2O3 − δ (BZY20) proton-conducting membranes, J. Electrochem. Soc. 165 (2018) F581, https://doi.org/10.1149/2.0161809jes.

[16] H. Ding, W. Wu, C. Jiang, Y. Ding, W. Bian, B. Hu, P. Singh, C.J. Orme, L. Wang, Y. Zhang, D. Ding, Self-sustainable protonic ceramic electrochemical cells using a triple conducting electrode for hydrogen and power production, Nat. Commun. 11 (2020) 1907, https://doi.org/10.1038/s41467-020-15677-z.

[17] C. Duan, D. Hook, Y. Chen, J. Tong, R. O'Hayre, Zr and Y co-doped perovskite as a stable, high performance cathode for solid oxide fuel cells operating below 500 °C, Energy Environ. Sci. 10 (2017) 176–182, https://doi.org/10.1039/C6EE01915C.

[18] J. Kim, S. Sengodan, G. Kwon, D. Ding, J. Shin, M. Liu, G. Kim, Triple-conducting layered perovskites as cathode materials for proton-conducting solid oxide fuel cells, ChemSusChem 7 (2014) 2811–2815, https://doi.org/10.1002/cssc.201402351.

[19] Y. Patcharavorachot, N.P. Brandon, W. Paengjuntuek, S. Assabumrungrat, A. Arpornwichanop, Analysis of planar solid oxide fuel cells based on proton-conducting electrolyte, Solid State Ionics 181 (2010) 1568–1576, https://doi.org/10.1016/j.ssi.2010.09.002.

[20] M. Bavarian, M. Soroush, Mathematical modeling and steady-state analysis of a proton-conducting solid oxide fuel cell, J. Process Control 22 (2012) 1521–1530, https://doi.org/10.1016/j.jprocont.2012.01.014.

[21] H. Liu, Z. Akhtar, P. Li, K. Wang, Mathematical modeling analysis and optimization of key design parameters of proton-conductive solid oxide fuel cells, Energies 7 (2014) 173–190, https://doi.org/10.3390/en7010173.

[22] A. Arpornwichanop, Y. Patcharavorachot, S. Assabumrungrat, Analysis of a proton-conducting SOFC with direct internal reforming, Chem. Eng. Sci. 65 (2010) 581–589, https://doi.org/10.1016/j.ces.2009.06.066.

[23] Y. Kalinci, I. Dincer, Analysis and performance assessment of NH3 and H2 fed SOFC with proton-conducting electrolyte, Int. J. Hydrogen Energy 43 (2018) 5795–5807, https://doi.org/10.1016/j.ijhydene.2017.07.234.

[24] V. Menon, A. Banerjee, J. Dailly, O. Deutschmann, Numerical analysis of mass and heat transport in proton-conducting SOFCs with direct internal reforming, Appl. Energy 149 (2015) 161–175, https://doi.org/10.1016/j.apenergy.2015.03.037.

[25] M. Ni, D.Y.C. Leung, M.K.H. Leung, Electrochemical modeling of ammonia-fed solid oxide fuel cells based on proton conducting electrolyte, J. Power Sources 183 (2008) 687–692, https://doi.org/10.1016/j.jpowsour.2008.05.018.

[26] M. Ni, M.K.H. Leung, D.Y.C. Leung, Electrochemical modeling of hydrogen production by proton-conducting solid oxide steam electrolyzer, Int. J. Hydrogen Energy 33 (2008) 4040–4047, https://doi.org/10.1016/j.ijhydene.2008.05.065.

[27] Y. Wang, B. Zu, R. Zhan, Q. Du, M. Ni, K. Jiao, Three-dimensional modeling and performance optimization of proton conducting solid oxide electrolysis cell, Fuel Cells 20 (2020) 701–711, https://doi.org/10.1002/fuce.201900246.

[28] H. Zhu, S. Ricote, W.G. Coors, R.J. Kee, Interpreting equilibrium-conductivity and conductivity-relaxation measurements to establish thermodynamic and transport properties for multiple charged defect conducting ceramics, Faraday Discuss 182 (2015) 49–74, https://doi.org/10.1039/C5FD00012B.

[29] J.-H. Zhang, L.-B. Lei, D. Liu, F.-Y. Zhao, M. Ni, F. Chen, Mathematical modeling of a proton-conducting solid oxide fuel cell with current leakage, J. Power Sources 400 (2018) 333–340, https://doi.org/10.1016/j.jpowsour.2018.08.038.

[30] H. Zhu, C. Karakaya, R.J. Kee, Modeling ammonia-fueled co-flow dual-channel protonic-ceramic fuel cells, Int. J. Green Energy 19 (2022) 1568–1582, https://doi.org/10.1080/15435075.2021.2018321.

[31] H. Zhu, R.J. Kee, Modeling protonic-ceramic fuel cells with porous composite electrodes in a button-cell configuration, J. Electrochem. Soc. 164 (2017) F1400–F1411, https://doi.org/10.1149/2.0591713jes.

[32] L. Lei, J. Zhang, R. Guan, J. Liu, F. Chen, Z. Tao, Energy storage and hydrogen production by proton conducting solid oxide electrolysis cells with a novel heterogeneous design, Energy Convers. Manag. 218 (2020) 113044, https://doi.org/10.1016/j.enconman.2020.113044.

[33] E. Vøllestad, H. Zhu, R.J. Kee, [NPP-Integral model comparison-on Word] Interpretation of Defect and Gas-Phase Fluxes through Mixed-Conducting Ceramics Using Nernst–Planck–Poisson and Integral Formulations, J. Electrochem. Soc. 161 (2013) F114, https://doi.org/10.1149/2.067401jes.

[34] D.-K. Lim, C.-J. Park, M.-B. Choi, C.-N. Park, S.-J. Song, Partial conductivities of mixed conducting BaCe0.65Zr0.2Y0.15O3–δ, Int. J. Hydrogen Energy 35 (2010) 10624–10629, https://doi.org/10.1016/j.ijhydene.2010.07.122.
[35] T. Norby, M. Widerøe, R. Glöckner, Y. Larring, Hydration hydrogen in oxides, Dalton Trans. (2004) 3012–3018, https://doi.org/10.1039/B403011G.
[36] L.P. Putilov, V.I. Tsidilkovski, The role of deep acceptor centers in the oxidation of acceptor-doped wide-band-gap perovskites ABO3, J. Solid State Chem. 247 (2017) 147–155. https://api.semanticscholar.org/CorpusID:100380841.
[37] H. Guo, Y. Li, L. Jiang, Y. Sha, S. Guo, D. Han, Transport properties of the Ba(Zr,Ce,Y,Yb)O3−δ proton conductor: the real role of co-substitution of Y and Yb, J. Mater. Chem. A 12 (2024) 5875–5884, https://doi.org/10.1039/D3TA07486B.
[38] D. Ferrero, G. Dealberti, S. Anelli, A. Baggio, D. Schmider, J. Dailly, F. Smeacetto, M. Santarelli, Modeling of a single repeating unit for protonic ceramic cell applications, ECS Trans. 111 (2023) 1185, https://doi.org/10.1149/11106.1185ecst.
[39] S. Choi, T.C. Davenport, S.M. Haile, Protonic ceramic electrochemical cells for hydrogen production and electricity generation: exceptional reversibility, stability, and demonstrated faradaic efficiency, Energy Environ. Sci. 12 (2019) 206–215, https://doi.org/10.1039/C8EE02865F.
[40] T. Norby, EMF method determination of conductivity contributions from protons and other foreign ions in oxides, Solid State Ionics 28 (1988) 1586–1591.
[41] W. Wang, D. Medvedev, Z. Shao, Gas humidification impact on the properties and performance of perovskite-type functional materials in proton-conducting solid oxide cells, Adv. Funct. Mater. 28 (2018) 1802592, https://doi.org/10.1002/adfm.201802592.
[42] L. Schley, V. Vibhu, L. Nohl, I.C. Vinke, L.G.J. (Bert) de Haart, R.-A. Eichel, A highly stable Pr2NiO4+δ oxygen electrode in electrolyte supported protonic ceramic electrolysis cells (PCECs) for hydrogen production with high faradaic efficiency, Energy Adv. 3 (2024) 861–873, https://doi.org/10.1039/D3YA00542A.
[43] L. Bi, E. Traversa, Steam electrolysis by proton-conducting solid oxide electrolysis cells (SOECs) with chemically stable BaZrO3-Based electrolytes, ECS Trans. 68 (2015) 3387, https://doi.org/10.1149/06801.3387ecst.
[44] Y. Tong, Y. Wang, C. Cui, S. Wang, B. Xie, R. Peng, C. Chen, Z. Zhan, Preparation and characterization of symmetrical protonic ceramic fuel cells as electrochemical hydrogen pumps, J. Power Sources 457 (2020) 228036, https://doi.org/10.1016/j.jpowsour.2020.228036.
[45] K. Nomura, H. Kageyama, Transport properties of Ba(Zr0.8Y0.2)O3 - δ perovskite, Solid State Ionics 178 (2007) 661–665, https://doi.org/10.1016/j.ssi.2007.02.010.